



Nuclear Materials Authority
P.O.Box 530 Maadi, Cairo, Egypt

ISSN 2314-5609
Nuclear Sciences Scientific Journal
8, 99- 115
2019
<http://www.ssnma.com>

HYPERSPECTRAL ANALYSIS OF ASTER AND LANDSAT 8 DATA TO CHARACTERIZE EL-MISSIKAT URANIUM BEARING SILICEOUS VEINS AND THEIR ANALOGY TO EL-ERADIYA AND GATTAR GRANITES, EASTERN DESERT, EGYPT

MOHAMED A. EL ZALAKY

Nuclear Materials Authority, P.O. 530 El-Maadi, Cairo, Egypt

ABSTRACT

This work aims to apply spectral image processing techniques that have been used often to process hyperspectral data to analyze multispectral ASTER (Advanced Spaceborne Thermal Emission and Reflection Radiometer) and Landsat 8 data for mapping uranium-bearing siliceous rocks within El-Missikat granite. These techniques succeeded effectively in recognition of the same features at El-Eradya and Gattar granites. Siliceous materials (siliceous sinter), as used here, is a spectral group of SiO_2 minerals including opal, chalcedony and cristobalite derived from hydrothermal fluids and/or the decomposition of granite. The spectral identification of such minerals depend mainly on the uses a hydration absorption feature that characterize some hydrated silica at wavelength region of 2.2- to 2.4- μm .

The effectiveness of the hyperspectral analysis techniques used to compare a pixel spectrum with the spectra of known pure materials, extracted from the spectral end member selection procedures, including minimum noise fraction (MNF), pixel purity index (PPI) and n-dimensional visualization. Among those of the spectral analysis algorithms employed, spectral angle mapping (SAM) and matched filtering (MF) produced accurate classifications that were close to the ground reference data. The hyperspectral analysis of an ASTER and Landsat 8 dataset covering the studied areas, has successfully effective in detecting lithological units than traditional multispectral analysis procedures.

Field validation and laboratory investigation were carried out to prove and support the results obtained from ASTER and Landsat 8 processing. These results succeeded to delineate additional sites of siliceous materials that could be a promising areas to host the uranium mineralization.

INTRODUCTION

Although, uranium as a valuable metal cannot be detected directly by any remote sensor, the presence of minerals which form in association with this valuable metal can be located based on their spectral signatures. A group of minerals which occur in the alteration zones associated with uranium deposits, generically referred as iron oxides, clay minerals, and siliceous materials have diagnostic spectral

signatures mostly in the visible-near infrared and shortwave infrared portions of the electromagnetic spectrum. These signatures can be used to locate sites most favorable to the occurrence of deposits, saving the mineral industry a great deal of time and costs in their exploration programs (Sabins, 1999).

The geological mapping and mineral exploration is one of the primary tasks of remote sensing. It provides a solution to overcome the

difficulties and limitation in inaccessible regions. Recently, remote sensing satellite data are commonly used for lithological mapping, structural analysis and mineral exploration around the world (Mars and Rowan 2006; Zhang et al. 2007; Pour and Hashim 2014 & 2015; Pournamdaryet al. 2014a & 2014b; Amer et al. 2016; Guha and Kumar 2016; Pour et al. 2017; Eldosouky et al. 2017; Noda and Yamaguchi 2017).

Imaging spectrometry technology is especially welcomed by many earth scientists because it is sensitive to the physical and chemical properties of materials, making it possible to identify the mineral constituents of the surface within the instantaneous-field-of-view (IFOV), (Chabrilat et al., 2000).

As a matter of fact, there is no universal agreement currently on the minimum number of bands beyond which a dataset can be called hyperspectral, although it is often assumed that hyperspectral data should contain bands with relatively narrow (<10nm) and often continuous bandwidths in the visible and near infrared (VNIR) spectral regions (Baltavia, 2002). Some of the hyperspectral techniques were not specifically devised for processing hyperspectral images (Green et al., 1988), and in many respects, are simply an extension of the techniques that were originally used for multispectral data. For these reasons, many of hyperspectral techniques can be applicable logically to multispectral data sets such as the present dataset of ASTER and Landsat 8 (Research Systems, Inc., 2002).

The main target of this paper is to employ spectral image processing techniques that have been used often to process hyperspectral data to analyze multispectral ASTER and Landsat 8 data for the purpose of spectrally mapping uranium-bearing siliceous rocks within El-Missikat granite, hoping that these techniques will succeed effectively in recognition the same features at El-Eradiya and Gattar granites. To achieve this goal, the nature and composition of siliceous materials that host the uranium mineralization at El-Missikat

granite must be considered. The following section will be introduce the previous description of these siliceous materials that occupied El-Missikat shear zone and mainly confined to the mineralization of uranium. The spectral image analysis techniques applied to the ASTER and Landsat 8 dataset of El-Missikat area, to characterized and delineate the siliceous materials, are explained and the results are described.

El-Missikat uranium prospect area is located at the northern part of Gabal (G.) El-Missikat. The latter is considered as the northwestern part of an elliptical shape pluton comprising G. El-Missikat in the northwest, G. Ria El-Garra in the east and G. El-Giddami in the south (El Zalaky, 2007), (Fig. 1). This pluton roughly shows elongation in NNW-SSE direction, nearly parallel to the Red Sea and geographically bounded by long. 33° 21' 4.7" to 33° 29' 19.3" E and lat. 26° 24'3.8" to 26° 29' 58.6"N.

GEOLOGICAL SETTING

The Nuclear Materials Authority programs led to the discovery of some uranium mineralization related to the so-called Younger Granites (YG, 550-590 Ma), in the Eastern Desert of Egypt. These post-tectonic younger granites of Egypt represent the magmatic activity marking the end of the cratonization process of the Pan-African Orogeny (El-Gaby et al., 1988). The younger granite plutons are affected by post-magmatic deuteric and hydrothermal alterations associated in many places by rare metal mineralizations (Hunting 1967, Bugrov et al. 1973, Sabet et al., 1973). Some of these plutons are hosts of uranium mineralization in the Eastern Desert of Egypt. Three of them, namely El-Missikat (Bakhit, 1978), El-Erediya (El-Kassas, 1974) and G. Gattar (Salman et al., 1990) plutons, the mineralizations considered as uranium vein-type (Hussien et al., 1986 and Roz, 1994) that structurally controlled by faults and their feather joints.

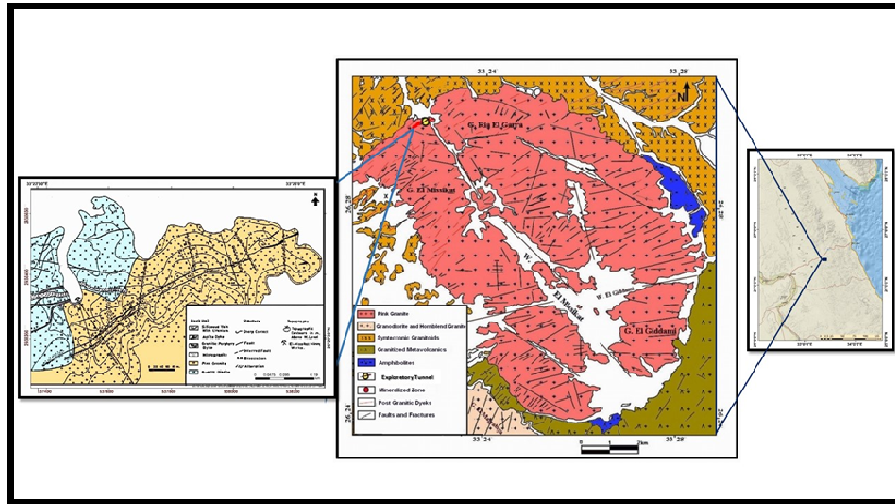


Fig.1: Geological map of Gabal El-Missikat area and its main uranium prospect (After Abou Deif, 1985 and El Zalaky, 2007)

Widespread silicification, hematitization, kaolinization and sericitization, as well as other alterations, accompany the uranium mineralization. Uranium is concentrated in the center of the mineralized faults and fractures together with jasper (in El-Erediya) or black silica and jasperoid veins (in El-Missikat) while in Gattar the uranium mineralization is confined to strong hematitization and to a lesser extent to quartz and jasperoid veins especially at the northern part of the pluton. Pitchblende is the primary mineral which suffered intensive oxidation and probably leaching, relics protected by silica was recorded in the three localities with different habit and concentration.

Regarding El-Missikat area, the granite of G. El-Missikat is essentially composed of alkali feldspars, quartz, and sodic plagioclase, with very subordinate amounts of biotite, sphene, apatite, zircon and opaque minerals. Iron oxides occur as clots of hematite and limonite. Silicification, sericitization, and kaolinization are also common. Across the northwestern slope of G. El-Missikat, an ENE trending shear zone extends southwestwards within the older granite and north-eastwards in G. El-

Garra (Fig.1). This shear zone is defined by a complicated system of siliceous veins which have a general ENE trend. The granite between the siliceous veins is highly brecciated, silicified and altered. Besides widespread silicification, sericitization and kaolinization are also common. Other siliceous veins also occur in several parts of G. El-Missikat and G. El-Garra, some with radiometric anomalies. Visible uranium minerals were recorded in this shear zone (Hussien et al., 1986 and Abou Dief, 1992).

Field observations revealed that uranium mineralization as well as high radioactivity are associated with the siliceous veins within and branching from the shear zone. These types of siliceous material can be distinguished into three types, namely light-colored silica, black silica and jasperized silica. The light-colored silica is micro- to cryptocrystalline while the latter two types are cryptocrystalline to amorphous. The black colored silica shows the maximum radioactivity and considered as the main host of the uranium minerals that distribute randomly within the silica (Fig.2). The jasperized silica has a deep to rose color, shows moderate radioactivity



Fig.2: Uranium mineralization (yellow) associated with the siliceous materials

and also contains a concentration of uranium minerals, less than the black one. Brecciation is very common in which both black and jasperized silica contain sub-angular fragments of granite and light-colored silica (Fig.3).

The author explained that this crypto-crystalline to amorphous silica (black and jasperoid silica) is similar in characters to the opalized silica, that formed during hot water circulates in the subsurface and dissolves silica from the host rock, in terms of it is dominantly consisted of amorphous SiO_2 (with a variable quantity of water), and a minor quantity of crystalline tridymite and quartz. Disordered structure of this material is a con-



Fig.3: Brecciated granite and white silica within the jasperoid silica veins

sequence of its genesis. Fast transition from liquid to solid state enables the existence of the dominant amorphous state (Boškovski et al., 2015). These mineral identifications have been confirmed in the field, optical transmission microscopy and with XRD (Attawiya, 1983). It is well known that Opal occur in a variety of species as opal-C (disordered cristobalite), opal-CT (disordered cristobalite and tridymite) and opal-A (amorphous opal) (Graetsch, 1994).

MATERIALS AND METHODS

Numerous geospatial data encompassing ASTER, OLI Landsat 8 satellite data, and other ancillary geological data such as geological maps are used in this study. The advanced space-borne thermal emission and reflection radiometer (ASTER) was launched onboard NASA's Terra spacecraft in December 1999. It covers a wide spectral region with 14 bands from the visible to the thermal infrared with high spatial, spectral and radiometric resolution. An additional backward-looking near infrared band provides stereo coverage. The spatial resolution varies with wavelength: 15 m in the visible and near-infrared (VNIR), 30 m in the shortwave infrared (SWIR), and 90 m in thermal infrared (TIR). The minimum revisits time interval over any given site is 16 days. Each ASTER scene covers an area of about 60 x 60 km. ASTER L1T product is a registered radiance at sensor data. So, several pre-processing techniques were applied on subset data covering the study areas to be suitable for further image processing techniques. These pre-processing techniques include cross-talk correction of ASTER-SWIR bands, layer stacking of VNIR-SWIR bands and corrected to surface reflectance using QUick Atmospheric Correction (QUAC). The OLI Landsat 8 data was selected because it has a number of bands greater than the Enhancement Thematic Mapper (ETM) (11 bands), also its relatively small ground resolution (30*30 m), moreover it has

high signal-to-noise radiometer performance, allowing 16-bit quantification of data. The following Table (Table 1) describe the characteristic feature of the remote sensing data set that used during this study.

These tools were used in the current study to characterize and map the uranium-bearing siliceous materials by applying the minimum noise fraction (MNF), pixel purity index (PPI) and n-dimensional visualization. Different type of spectral analysis algorithms employed, spectral angle mapping (SAM) and matched filtering (MF) to eliminate the similar probable sites of mineralization by using ENVI 5.3 and ArcGIS 10.5 software. The field verification and laboratory examination of selected samples are very important step to verify the detected promising radioactive anomalies.

RESULT AND DISCUSSION

The possibility to construct a spectrum for each pixel in the image is commonly based on the fact that remotely sensed imagery is sampled with numerous spectral bands at narrow band widths. The spectra of the endmembers can be extracted from image derived “pure pixels”(Qiu et al., 2006). Therefore, this work aim to extract the end-members derived from the image using pixel purity index and n-dimensional visualization procedures for the subsequent analyses that led to discriminate the siliceous materials (veins) that associated with the uranium mineralization.

To effectively extract endmembers from high dimensional remote sensing data such ASTER and Landsat 8, it is often necessary to decrease the dimensionality of the original data and segregated the noise. This is often achieved by applying a minimum noise fraction (MNF) transformation to the high dimensional data (Elnagdy and Abdelsalam, 2006).

Once the inherent dimensionality of the image data is determined using the MNF transform, endmembers can then be derived by using pixel purity index and n-dimensional visualization techniques from the higher-order MNF Eigen images. These endmembers can be compared subsequently with the remote sensing data to determine the surface materials of each pixel by employing one of the spectral analysis algorithms, such as Spectral Angle Mapper (SAM), and Matched Filtering (MF). Spectral Angle Mapping and Matched filtering techniques were applied by many researchers in remote sensing studies (Boardman and Kruse 1994, Van Der Meer and De Jong, 2001, Rowan et al., 2003, Qui et al., 2006, Daryani, et al., 2015 and Akbari, et al., 2015). The techniques used in ASTER and Landsat 8 data processing are described below.

Minimum Noise Fraction (MNF) Transform

The MNF transform is composed of two consecutive principal component (PC) transforms (Green et al., 1988). The first PC

Table 1: The characteristic feature of the remote sensing data used in this work

Satellite	Level	Scene ID.	Covered Area
Landsat-8	L1TP	LC08_L1TP_175041_20170604_20170616_01_T1	Gattar pluton
Landsat-8	L1TP	LC08_L1TP_174042_20170816_20170825_01_T1	El-Missikat and El-Eradiya plutons
ASTER	AST_L1T	AST_L1T_0030310200608351_9_20150513120945_26196	El-Missikat and El-Eradiya plutons
ASTER	AST_L1T	AST_L1T_0030310200608351_0_20150513120937_117085	Gattarpluton

transform focuses on whitening noise by decorrelating and rescaling the noise in the data, producing data in which the noise has unit variance and no band-to-band correlations (Green et al., 1988). The transformed noise whitened data are then subjected to a second standard PC transform, giving rise to final outputs that are not correlated and are arranged in terms of decreasing information content (Research Systems, Inc., 2002). The eigenvalues of the output MNF eigenimages of the ASTER and Landsat 8 data of El-Missikat area are displayed on Figure 4 and extracted to improve the subsequent spectral processing results, MNF components with eigenvalues less than 1 are usually excluded from the data as noise since eigenimages with near-unity eigenvalues are normally noise-dominated (Jensen, 2005).

The MNF transform applied to the both ASTER and Landsat 8 data achieved a reasonable separation of coherent signal from complementary noise, therefore the MNF transformed eigenimages were employed and coupled with pixel purity index and n-dimensional visualization techniques to facilitate the extraction of the endmembers.

Pixel Purity Index

Most pixels often contain varying proportions of different materials of more than one

type of the surface materials, so the identifying of endmember pixels whose spectra are extreme (or spectrally pure) is not a simple task, especially in high-dimension image datasets. The extraction of endmembers often has to be based on rigorous mathematical algorithms, such as pixel purity index.

Pixel purity index (PPI) is a means to determine the relative purity of the pixels from the higher order MNF eigenimages using the convex geometry argument (Boardman, 1993; Boardman et al., 1995). PPI image is formed by repeatedly projecting n-dimensional scatter plots of the MNF images onto a random unit vector, so the pixel value corresponds to the total number of times that the pixel was judged as "extreme" (i.e., falling onto the ends of the unit vector) in all projections. Finally, the brighter the pixel in the PPI image the higher the relative purity because it was more frequently recorded as being a spectrally extreme pixel. 10,000-projection of the scatter plot and a threshold factor of 2.5 is applied to the PPI image to select the purest PPI pixels (EXELISVIS ENVI, 2015). The PPI is performed on the MNF components extracted from both ASTER and Landsat-8 bands covering El-Missikat area. The image of PPI of El-Missikat area reveals that the land surface with mixed materials appear as dark (low PPI) while the area of pure material appears as high bright pixel in PPI image (Fig.5).

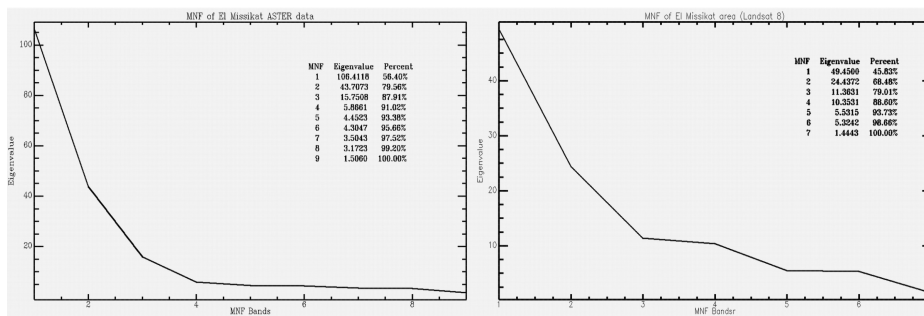


Fig.4: The MNF eigenvalues plot of the eigenimages of ASTER (left) and Landsat-8 (right) data of El-Missikat area

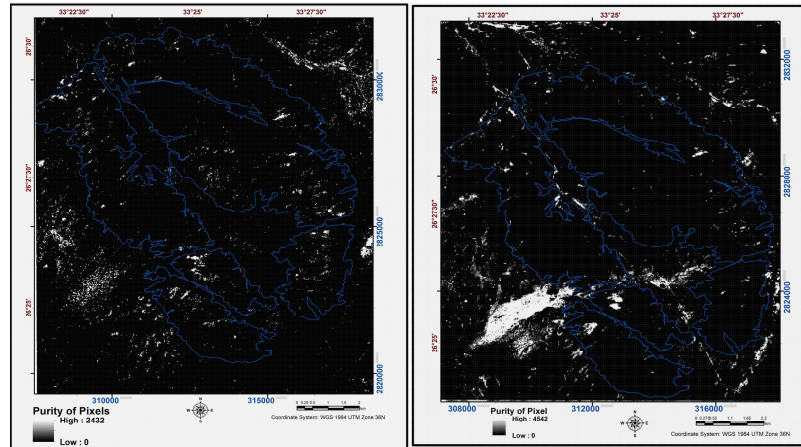


Fig. 5: Pixel Purity Index (PPI) map of El-Missikat ASTER (left) and Landsat 8 (right) MNF images

N-Dimensional Visualization and Endmember Extraction

Jensen 2005 suggested an interactive tool for endmembers identification using n-dimensional visualizer. This tool depends mainly on the plotting the DN of pixels of the MNF coherent images on orthogonal axes and the DN of each pixel in the coherent image is plotted as a discrete point. This creates a data cloud in the n-dimensional space in which the mixed pixels are plotted in the interior of this data cloud whereas the more pure pixels are located at the edges of the data cloud and could be taken as endmember (Kruse, 1997). Usually, the number of endmembers that can be extracted is equal to the number of the MNF components image plus one (Boardman, 1993).

Ten and eight endmembers extracted automatically from both ASTER and Landsat 8 of El-Missikat data respectively could be identified. These endmembers are corresponding to the surface materials (different rock types) at El-Missikat area such as younger granite, older granite, metavolcanic, amphibolites, siliceous materials that occupied the uranium shear zone, kaolinite alteration and other different rock types according to the extracted end-

members (Fig.6). Some of these endmembers were probably assigned to the rock type depend on the previous mapping of this area (Abou Dief, 1992 and El Zalaky, 2007) while the other considered as undefined types.

Spectral Angle Mapper (SAM)

Spectral Angle Mapping (SAM) technique suggested by Kruse et al. (1993), is a supervised classification depends on the angles between image pixel spectra and training data (ROIs) spectra or library spectra (extracted endmembers in this case). The algorithm determines the similarity between two spectra by calculating the spectral angle between them. SAM compares the angle between the endmember spectrum vector and each pixel spectrum vector in n-dimension space. Smaller angles represent closer matches to the reference spectrum. Pixels further away than the specified maximum angle threshold in radians are not classified. The pixel with smaller spectral angle appears darker indicating a higher match to that specific reference spectrum (Research Systems, Inc. 2002; Jensen, 2005). In order to extract thematic information from the ASTER and Landsat 8 images of the studied areas, it is often necessary to

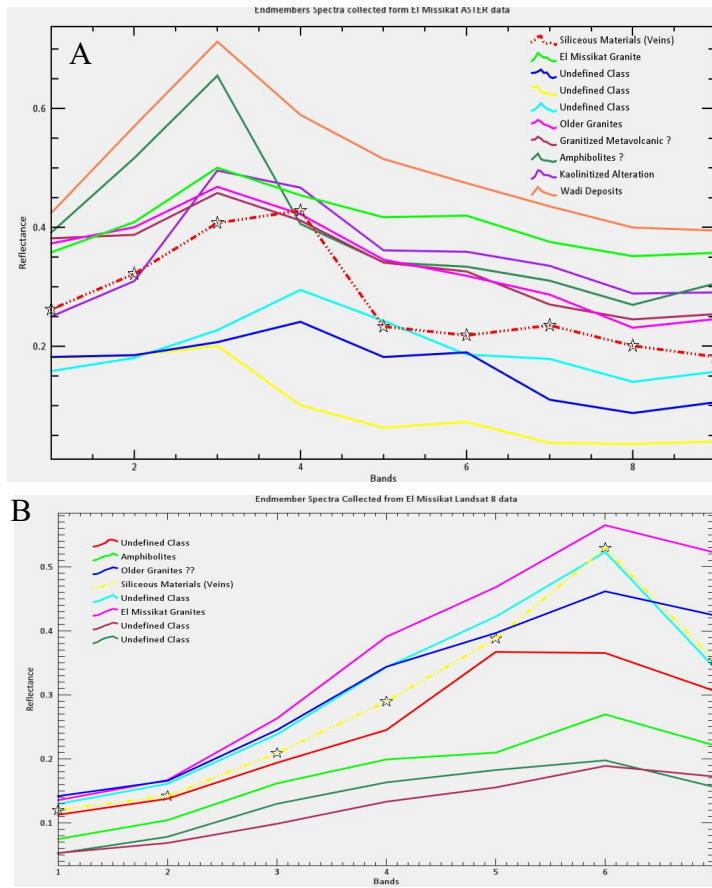


Fig.6: The spectral curves of the extracted endmembers of ASTER data (A) and Landsat 8 data (B)

compare individually each unclassified pixel of the image with the image-derived reference spectra (endmembers) extracted from El-Missikat data and then determine which reference spectrum most closely resembles the spectral characteristics of the pixel. The result is a classification image and a rule image for each endmember. The SAM classification images of both ASTER and Landsat 8 data are successfully delineate different rock types of El-Missikat areas in addition to recognize the siliceous materials that appear in red and yellow color respectively (Fig.7 A & B). The endmember corresponding to the siliceous ma-

terials was specially provided in the field (Fig. 8 & 9) and will be used as reference spectral for the subsequent hyperspectral techniques and to recognize the same features in Gattar and El-Eradiya granites.

By applying the SAM algorithm on the ASTER and Landsat 8 dataset of both Gattar and El-Eradiya areas, setting the maximum angle (radians) area equal (0.5), using only the selective endmember that characterized the siliceous materials to create a gray-scale rule image corresponding to the similarity between the reference endmember and to the target area. The pixels with smaller spectral

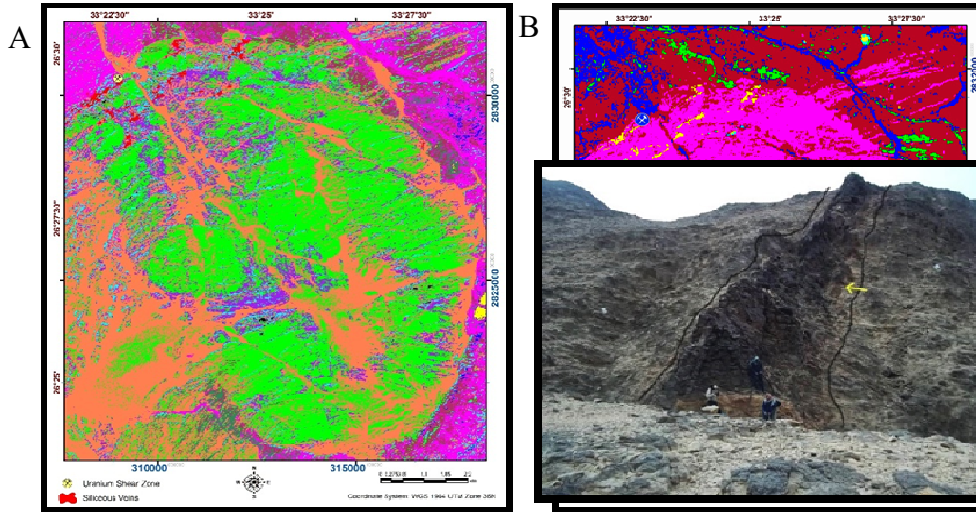


Fig.7: Results of applying SAM supervised classification technique using ASTER data (A) and Landsat 8 data, (B) to delineate the siliceous materials (veins), by red and yellow color respectively, El-Missikat shear zone



Fig.8: Silicified zone invaded El-Missikat mineralized shear zone



Fig. 9: Silicified zone extended to upper part of El-Missikat mineralized shear zone

angle appear darker indicating a higher match to that siliceous materials endmember.

The threshold anomaly of the SAM image can be generated by using density slice in ENVI software with confidence range from 97 to 95% (mean plus three times standard deviation or mean plus two times the standard deviation). The result displayed overlaid on the RGB color composite image 864 and 753

of both ASTER and Landsat 8 data respectively (Figs.10 and 11). It's found that the SAM image can successfully define the siliceous materials zones within Gattar pluton at southwestern part of G. Umm Disi and some localities at G. Abou Al Hasan Al Ahmer that marked by circles in both image (Fig.10 A and B). While in El-Eradiya granites, zones of siliceous materials appear by red color (left

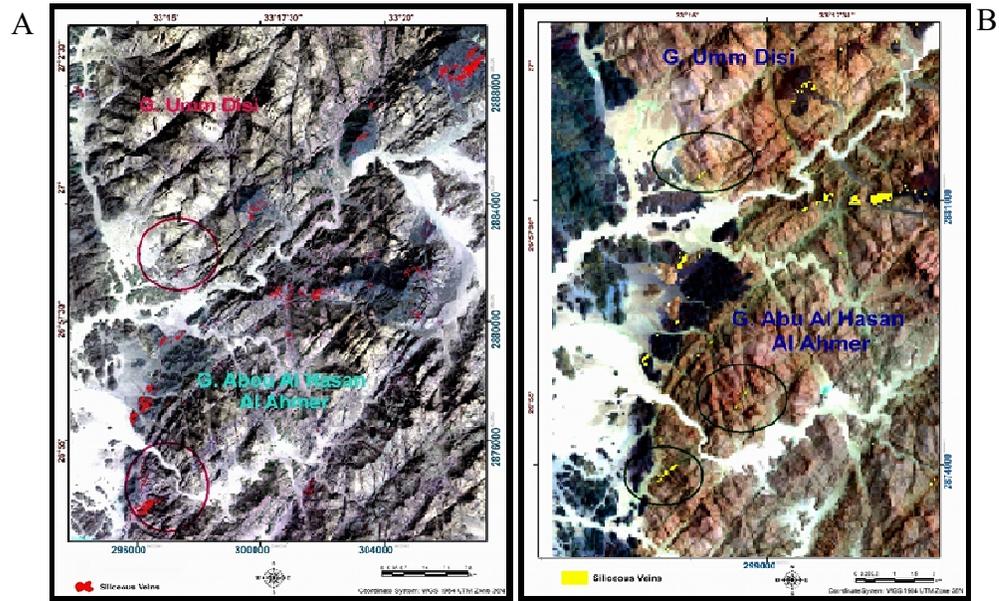


Fig.10: RGB images show the results of applying SAM technique using ASTER data (A) and Landsat 8 data, (B) to delineate the siliceous materials (veins), Gattar granite

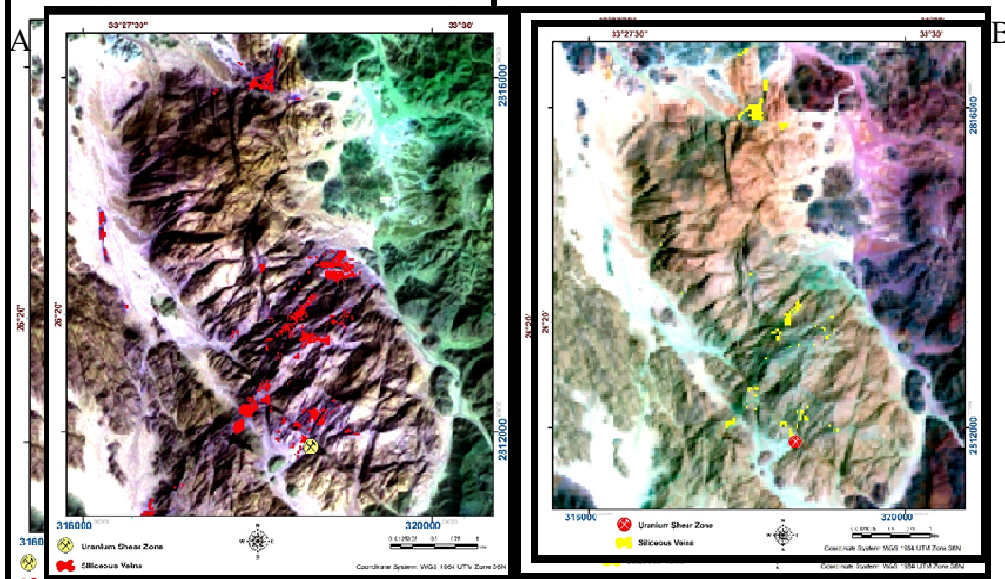


Fig.11: RGB images show the results of applying SAM technique using ASTER data (A) and Landsat 8 data, (B) to delineate the siliceous materials (veins), El-Eradiya granite

image) and yellow color (right image) at the central part of the pluton and around the uranium prospect area of El-Eradiya in addition to locality at the extreme north eastern part of the pluton.

Matched Filtering (MF)

Matched Filtering is a spectral technique that originally developed to compute the abundance of rare targets and to provide a rapid means of detection specific minerals based on their matching to the endmember reflectance spectra (Kruse, 1997 and Shippert, 2003). It also maximized the response of a known endmember and suppresses the response of the mixed unknown background (Harsanyi and Chang, 1994 and Kruse, 1997).

The result of applying MF technique on the data covering the investigated area is a gray scale images where the bright pixels represent a perfect match and good similarity to the siliceous endmember spectral reference.

The bright pixel converted to color slice depend on the threshold of confidence used in SAM technique. Figures (12 & 13) delineate and highlight the siliceous materials better than SAM technique at the same localities previously mentioned in both Gattar and El-Eradiya granite.

All the data images extracted from the different hyperspectral analysis were proved during the field work to achieve ground truth for this technique. The field observation revealed that most of these siliceous materials have a relatively higher in radioactivity than the surrounding rocks types especially when they intruded the granites. No visible uranium mineralization was recorded but the collected samples of the siliceous materials itself and the wall-rocks alteration adjacent to the siliceous materials at the southwestern part of G. Umm Disi showed a relatively high in radioactivity for all different kind of alteration such as kaolinization and partially

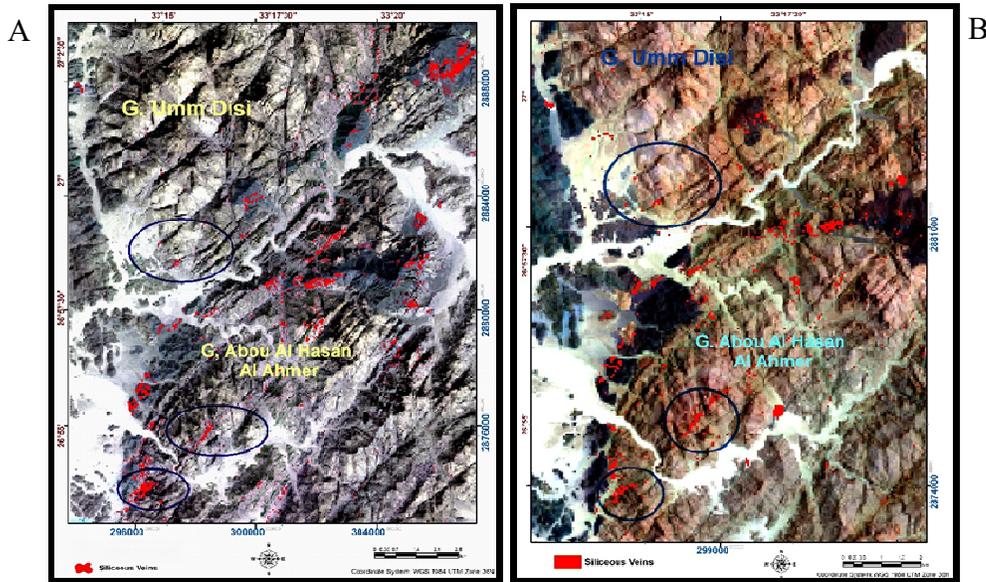


Fig.12: RGB images show the results of applying MF technique using ASTER data (A) and Landsat 8 data, (B) to delineate the siliceous materials (veins), Gattar granite

episyenitization (Figs.14 ,15 and 16). Most of the siliceous materials that delineated at El-Eradiya granite are located at zones of high and rugged topography and can't be reached easily while few zones are in the level of the wadi and not represent a significant area for uranium mineralization (Fig.17). The samples of the siliceous materials and their adjacent rocks are examined under environmental

scanning electron microscope (ESEM) that revealed the presence of uranium mineralization occurs as very fine inclusions invading and filling the vugs and microfracture in both the siliceous materials and kaolinitized zone at the southernwestern part of Gabal Umm Disi that recognized by remote sensing analysis (Fig.18).

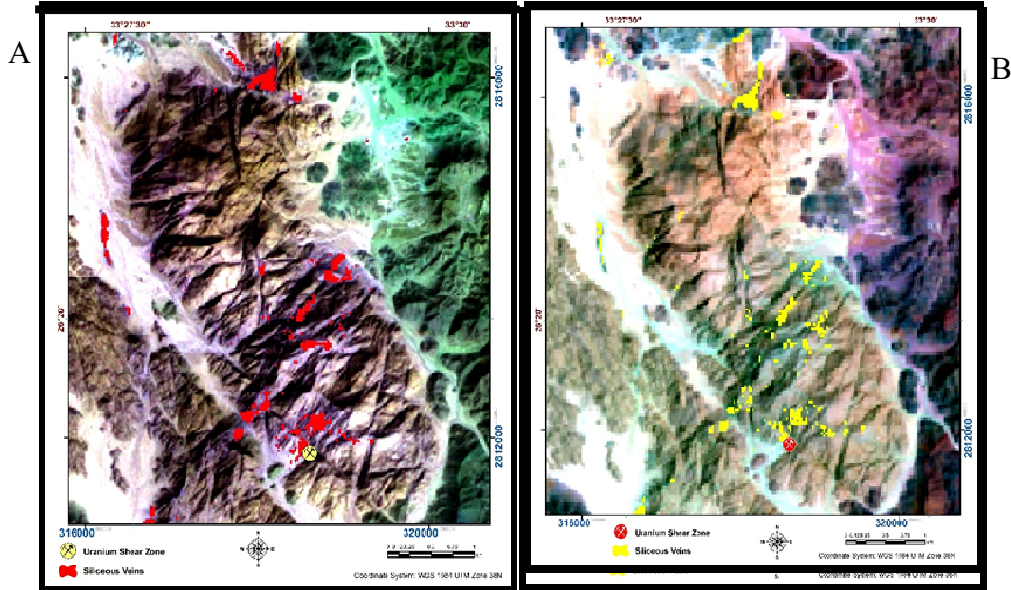


Fig.13:RGB images show the results of applying MF technique using ASTER and (A) and Landsat 8 data, (B) to delineate the siliceous materials (veins), El-Eradiya granite



Fig.14:Siliceous materials intruded to the granite southwestern part of Gabal Umm Disi



Fig.15:Kaolinitized alteration affecting the granite southwestern part of Gabal Umm Disi



Fig.16:Partially episyenitized granite, Southern part of Gattar pluton

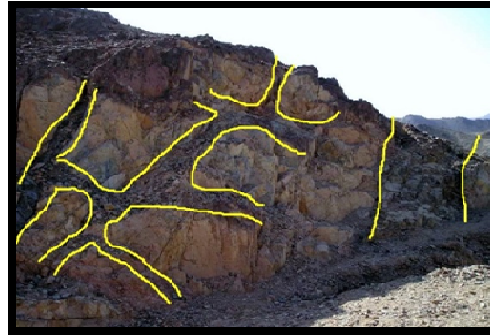


Fig.17:Siliceous materials intruded to El-Eradiya granite

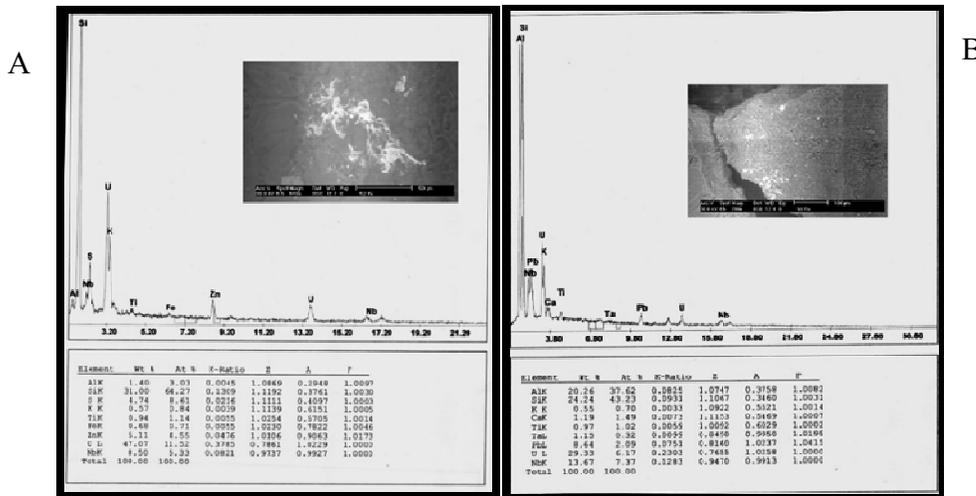


Fig.18:EDX and BSE image showing uranium mineralization (bright tone) associated with siliceous materials (A) and kaolinite alteration, (B) southwestern part of Gabal Umm Disi

CONCLUSION AND RECOMMENDATION

The improved spatial and spectral characteristics of multi spectral ASTER and Landsat 8 data have allowed the use of hyperspectral digital image processing techniques. Hyperspectral analysis of these data covering the study areas has resulted in significant

improvement of the hydrothermal alteration (siliceous materials) mapping of these areas.

Also, it can be evaluated the applicability of ASTER and Landsat-8 data for obtaining geological information on hydrothermal alteration (siliceous veins) associated with uranium deposits, with selected image-processing methods.

The hyperspectral techniques significantly yielded spectral information that allowed identification of new localities of siliceous materials in both Gattar and El-Eradiya pluton and become useful in the exploration of uranium mineralization.

Finally, this study concludes that hyperspectral analysis of ASTER and Landsat-8 image using reference spectra are a stable and reproducible technique for mapping siliceous materials (veins) as hydrothermal alteration products in arid areas such as the study area.

This study suggests that collecting field reflectance spectra of the siliceous materials and alteration zones to create a laboratory spectral endmembers of field samples. The collected spectra can be used for ASTER and Landsat-8 image classification.

REFERENCES

- Abou Dief, A., 1992. The Relation between Uranium Mineralization and Tectonics in some Pan-African Granites, west of Safaga, Eastern Desert, Egypt. Ph.D. Thesis, Assiut Univ., Egypt. 218p.
- Akbari, Z.; Rasa, I.; Mohajjel, M.; Adabi, M. H., and Yarmohammadi, A., 2015. Hydrothermal Alteration Identification of Ahangaran Deposit, West of Iran Using ASTER Spectral Analysis. *Inter. Geoinformatics Research and Development J.*, 6(1), 28-42.
- Amer, R.; El Mezayen, A. and Hasanein, M., 2016. ASTER spectral analysis for alteration minerals associated with gold mineralization. *Ore Geol Rev.*, 75, 239-251.
- Attawiya, M.Y., 1983. Mineralogical study of El-Eradiya uranium mineralization, Eastern Desert, Egypt. *Arab. J. Nucl. Sci. Tech.*, 2, 221-234.
- Bakhit, F.S., 1978. Geology and radioactive mineralization of Gebel El-Missikat area. Eastern Desert, Egypt, Ph.D. Thesis, Ain Shams Univ., Cairo, 280p.
- Baltsavia, E.P., 2002. Special section on image spectroscopy and hyperspectral imaging. *ISPRS J. of Photogrammetry and Remote Sensing*, 57, 169-170.
- Boardman, J.W., 1993. Automating spectral unmixing of AVIRIS data using convex geometry concepts. In: *Summaries of the 4th Annual JPL Air-borne Geoscience Workshop*, Pasadena, 11-14.
- Boardman, J.W., and Kruse, F.A., 1994. Automatic spectral analysis: a geological example using AVIRIS data, North Grapevine Mountain, Nevada. In: *10th Thematic Conf. on Geologic Remote Sensing*, Ann Arbor, 407-418.
- Boardman, J.W.; Kruse, F.A., and Green, R.O., 1995. Mapping target signatures via partial unmixing of AVIRIS data. In: *Summaries of the Fifth JPL Airborne Earth Science Workshop* (Jakob, V.Z., Ed.), 3. J. P. L, Pasadena, CA, , 23-26.
- Boškovski, B.; Bogoevski, S.; Ruseska, G., and Atkovska, K., 2015. High Temperature Crystallization Process Into Opalized Tuff. *Geologica Macedonica*, 29 (2), 209-213.
- Bugrov, V.A.; Abou El Gadael, A., and Soliman, M.M., 1973. Rare metallic albitites as a new type of ore mineralization in Egypt, *Annals Geol. Surv. Egypt*, 3, 185-206.
- Chabrilat, S.; Pinet, P.C.; Ceuleneer, G.; Johnson, P.E., and Mustard, J.F., 2000. Ronda peridotite massif: Methodology for its geological mapping and lithological discrimination from airborne hyperspectral data. *Inter. J. of Remote Sensing*, 21, 2363-2388.
- Daryani, N.J.; Arian, M., and Omran, N.R., 2015. Tectonics and Mineralisation of Copper in the Ardestan-Kahang Area, Central Iran by Remote Sensing. *Open J. Geol.*, 5(4), 188-196.
- El Zalaky, M.A., 2007. Geology and remote sensing studies on some uranium-bearing granites, Eastern Desert, Egypt. Ph.D. Thesis, Fac. Sci, Banha Univ, Egypt, 205p.
- Eldosouky, A.M.; Abdelkareem, M., and Elkha-

- teeb, S.O., 2017. Integration of remote sensing and aeromagnetic data for mapping structural features and hydrothermal alteration zones in Wadi Allaqi area, South Eastern Desert of Egypt. *J. Afr. Earth Sci.*, 130, 28-37.
- El-Gaby, S.; List, F.K., and Tehrani, R., 1988. Geology, evolution and metallogenesis of the Pan-African belt in Egypt. In: *The Pan-African of Northeast Africa and Adjacent Areas*(El-Gaby, S., Greiling, O.,Eds.), Fieder. Vieweg und Sohn, Braunschweig-Wiesbaden, Germany, 17-68.
- EL-Kassas, I.A., 1974. Radioactivity and geology of Wadi Atalla area, Eastern Desert of Egypt, Ph.D. Thesis, Ain Shams Univ., Cairo, 502p.
- Elnagdy, S.M., and Abdelsalam, M.G., 2006. Hyperspectral Analysis of the Advanced Spaceborne Thermal Emission and Reflection Radiometer (ASTER) Data: An Example from the Neoproterozoic Um Nar Banded Iron Formation (BIF), Egypt. *Egyptian J. Remote Sensing and Space Sci.*, 9, 53-78.
- EXELISVIS ENVI, 2015. Manual.
- Graetsch, H., 1994. Structural characteristics of opaline and microcrystalline silica minerals. In: *Silica-Physical Behavior, Geochemistry, and Materials Applications*(Gibbs, G.V.,Ed.), Review Mineralogy, Mineralogical Society of America, 29, 209–232.
- Green, A.A.; Berman, M.; Switzer, P., and Craig, M.D., 1988. A transformation for ordering multispectral data in terms of image quality with implications for noise removal. *IEEE Transactions on Geoscience and Remote Sensing*, 26, 65-74.
- Guha, A., and Kumar, V.K., 2016. Comparative analysis on utilisation of linear spectral unmixing and band ratio methods for processing ASTER data to delineate bauxite over a part of Chotonagpur plateau, Jharkhand, India. *Geocarto Int.*, 31(4), 367–384.
- Harsanyi, J.C., and Chang, C.I., 1994. Hyperspectral image classification and dimensionality reduction: An orthogonal subspace projection approach. *IEEE Transactions on Geosci. and Remote Sensing*, 32, 779-785.
- Hearn, D.R.; Digenis, C.J.; Lencioni, D.E.; Mendenhall, J.A.; Evans, J.B., and Walesh, R.D., 2001. EO-1 advanced land imager overview and spatial performance, *IEEE Trans. Geosci. And Remote Sensing*, 2, 897-899.
- Hunting Geology and Geophysics LTD, 1972. Assessment of the mineral potential of the Aswan Region, U.A.R. Photo- geological Survey, Hunting Geology and Geophysics Ltd.
- Hussien, H.A.; Hassan, M.A.; El Tahir, M.A., and Abou Deif, A., 1986. Uranium-bearing siliceous veins in younger granites, Eastern Desert, Egypt. *IAEA-TECDOC-361*, Vienna, 143-157.
- Jensen, J.R., 2005. *Introductory digital image processing*. Upper Saddle River, NJ: Pearson Prentice Hall, 278p.
- Kruse, F.A., 1997. Regional Mapping Along the Colorado River Front Range From FT Collins to Denver Using the Airborne Visible/Infrared Imaging Spectrometer (AVIRIS). 12th Inter. Conf. Applied Geol. Remote Sensing (Denver Colorado), 2, 91-98
- Kruse, F.A.; Lefkoff, A.B.; Boardman, J.W.; Heidebrecht, K.B.; Shapiro, A.T.; Barloon, P.J., and Goetz, A.F.H., 1993. The Spectral Image Processing System (SIPS), interactive visualization and analysis of imaging spectrometer data. *Remote Sensing Environ*, 44, 145–163
- Mars, J.C., and Rowan, L.C., 2006. Regional mapping of phyllic- and argillic-altered rocks in the Zagros magmatic arc, Iran, using Advanced Spaceborne Thermal Emission and Reflection Radiometer (ASTER) data and logical operator algorithms. *Geosphere*, 2(3), 161–186.
- Noda, S., and Yamaguchi, Y., 2017. Estimation of surface iron oxide abundance with suppression of grain size and topography effects. *Ore Geol. Rev.*, 83, 312–320
- Pour, A.B., and Hashim, M., 2015. Integrating PALSAR and ASTER data for mineral depos-

- its exploration in tropical environments: a case study from Central Belt, Peninsular Malaysia. *Int. J. Image Data Fusion*, 6(2), 170–188.
- Pour, A.B., and Hashim, M., 2014. ASTER, ALI and Hyperion sensors data for lithological mapping and ore mineral exploration. *Springerplus*, 3(130), 1-19.
- Pour, A.B.; Hashim, M.; Park, Y., and Hong, J. K., 2017. Mapping alteration mineral zones and lithological units in Antarctic regions using spectral bands of ASTER remote sensing data. *Geocarto Inter.*, 32(1), 1-26.
- Pournamdary, M.; Hashim M., and Pour AB., 2014a. Application of ASTER and Landsat TM data for geological mapping of Esfandagheh ophiolite complex, southern Iran. *Resour Geol.*, 64(3), 233–246.
- Pournamdary, M.; Hashim M., and Pour AB., 2014b. Spectral transformation of ASTER and Landsat TM bands for lithological mapping of Soghan ophiolite complex, south Iran. *Adv Space Res.*, 54(4), 694-709.
- Qiu, F.; Abdelsalam, M., and Thakkar, P., 2006. Spectral analysis of ASTER data covering part of the Neoproterozoic Allaqi-Heiani suture, Southern Egypt. *J. Afri. Earth Sciences*, 44(2), 169-180.
- Research Systems, Inc., 2002. ENVI Tutorials. Research Systems, Inc., Boulder, CO, 640p.
- Rowan, L.C.; Hook, S.J.; Abrams, M.J., and Mars, J.C., 2003. Mapping hydrothermally altered rocks at Cuprite, Nevada, using the Advanced Spaceborne Thermal Emission and Reflected Radiometer (ASTER), a new satellite-imaging system: *Economic Geology*, 98, 1019-1027.
- Roz, M.E., 1994. Geology and uranium mineralization of Gabal Gattar area, North Eastern Desert, Egypt. M.Sc. Thesis, Fac. Sci., Al Azhar Univ., 175p.
- Sabet, A.H.; Chabanenco, V., and Tsogoev, V., 1973. Tin-tungsten and rare metal mineralization in central Eastern Desert of Egypt. *Annals. Geol. Surv. Egypt*, 3, 75-86.
- Sabins, F.F., 1999. Remote sensing for mineral exploration. *Ore Geol. Rev.*, 14, 157-183.
- Salman, A.B.; El Aassy, I.E., and Shalaby, M.H., 1990. New occurrence of uranium mineralization in Gabal Qattar, Northern Eastern Desert, Egypt. *Ann. Geol. Surv. Egypt*, XVI, 31-34.
- Shippert, P., 2003. Introduction to hyperspectral image analysis. *Online J. Space Communication*, 3,13.
- US Geological Survey, 2012. Landsat Data Continuity Mission, US Geological Survey, Washington, DC,.
- Van Der Meer, F., and De Jong S.M., 2001. Remote sensing and digital image processing. *imaging spectroscopy Kluwer Academic publited in the Netherlands*, 4, 306p.
- Yamaguchi, Y.; Kahle, A.B.; Tsu, H.; Kawakami, T., and Pniel, M., 1998. Overview of advanced spaceborne thermal emission reflectance radiometer, *IEEE TGARS*, 36, 1062-1071.
- Zhang, X.; Pazner, M., and Duke, N., 2007. Lithologic and mineral information extraction for gold exploration using ASTER data in the south Chocolate Mountains (California). *J. Photogramm Remote Sens.*, 62, 271–282.
-

تطبيق تحليل غزير الأطياف لبيانات الأستر والاندسات ٨ لتمييز عروق السيلكا الحاوية لليورانيوم بالمسيكات لتحديد نظيرها بجرانيت العرضية وجرانيت جتار، الصحراء الشرقية، مصر

محمد على الزلقى

يهدف هذا العمل إلى تطبيق تقنيات معالجة الصور غزيرة الاطياف والتي تم استخدامها في كثير من الأحيان وذلك لمعالجة البيانات الطيفية لتحليل الأطياف متعددة الأطياف لبيانات الأستر وبيانات لاندسات ٨ لرسم صخور السيلكا الحاوية لليورانيوم داخل جرانيت المسيكات. نجحت هذه التقنيات بفعالية في التعرف على نفس الخصائص في كل من جرانيت العرضية وجرانيت جتار. المواد السليكاتية (siliceous sinter)، كما هو مستخدم هنا، هي مجموعة طيفية من معادن SiO_2 بما في ذلك الاوبال والكالسيوم والكرستوباليت والتي نشأت من تحلل الجرانيت بواسطة محاليل السوائل الحارمائية. إن التحديد الطيفي لهذه المعادن يعتمد بشكل رئيسي على استخدام خاصية امتصاص الماء التي تميز بعض السيلكا المائبة في منطقة الطول الموجي من ٢,٢ إلى ٢,٤ ميكرومتر.

تعتبر فعالية تقنيات التحليل غزير الأطياف في استخدام مقارنة طيف البيكسل مع أطراف المواد النقية المعروفة، المستخرجة من إجراءات اختيار (endmember)، بمساعدة كل من الحد الأدنى للضوضاء (MNF)، مؤشر نقاء البكسل (PPI) والتصور متعدد الأبعاد (n-dimensional visualization). فمن بين تلك الخوارزميات المستخدمة في التحليل الطيفي، (SAM) و (MF) والذي ينتج عنهما تصنيفات دقيقة كانت قريبة من البيانات المرجعية الأرضية. وقد نجح التحليل غزير الأطياف والذي طبق على بيانات الأستر والاندسات ٨ التي تغطي المناطق المدروسة في اكتشاف الوحدات الحجرية بنجاح أكبر من إجراءات التحليل التقليدية المتعددة الأطياف.

تم إجراء التحقق الميداني والفحص المختبري لإثبات ودعم النتائج التي تم الحصول عليها من معالجة بيانات الأستر والاندسات ٨. وقد نجحت هذه النتائج في تحديد مواقع إضافية من المواد السيليسية التي يمكن أن تكون منطقة واحدة لاستضافة تمعدنات اليورانيوم.